Self-annealing in a two-phase Pb-Sn alloy after processing by high-pressure torsion

Nian Xian Zhang, Nguyen Q. Chinh, Megumi Kawasaki, Yi. Huang, Terence G. Langdon

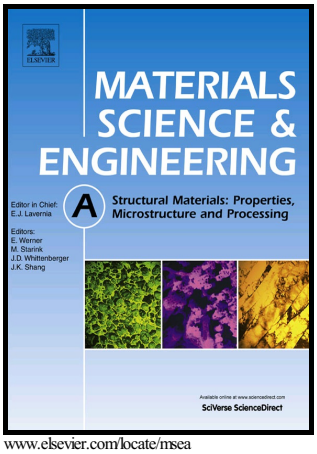

www.elsevier.com/locate/msea

PII: S0921-5093(16)30444-0
DOI: http://dx.doi.org/10.1016/j.msea.2016.04.058
Reference: MSA33587

To appear in: *Materials Science & Engineering A*

Received date: 4 April 2016
Revised date: 20 April 2016
Accepted date: 20 April 2016

Cite this article as: Nian Xian Zhang, Nguyen Q. Chinh, Megumi Kawasaki, Yi Huang and Terence G. Langdon, Self-annealing in a two-phase Pb-Sn alloy afte processing by high-pressure torsion, *Materials Science & Engineering A* http://dx.doi.org/10.1016/j.msea.2016.04.058

Self-annealing in a two-phase Pb-Sn alloy after processing by high-pressure torsion

Nian Xian Zhang[a], Nguyen Q. Chinh[b], Megumi Kawasaki[c,d], Yi Huang[a,*], Terence G. Langdon[a, d]

[a]Materials Research Group, Faculty of Engineering and the Environment,University of Southampton, Southampton SO17 1BJ, U.K

[b]Department of Materials Physics, Eötvös Loránd University, 1117 Budapest, Pázmány Péter s. 1/A., Hungary

[c]Division of Materials Science and Engineering, Hanyang University, Seoul 133-791, South Korea

[d]Departments of Aerospace & Mechanical Engineering and Materials Science,University of Southern California, Los Angeles, CA 90089-1453, U.S.A.

[*]Corresponding author. Y.Huang@soton.ac.uk

Abstract

A Pb-62% Sn two-phase eutectic alloy was processed by high-pressure torsion (HPT) and stored at room temperature (RT) to investigate the occurrence of self-annealing. The microstructural characteristics and mechanical properties were recorded during self-annealing using scanning electron microscopy, tensile testing and nanoindentation. Processing by HPT produces a weakening effect but storage at RT leads to a gradual increase in the hardness together with significant grain growth. Nanoindentation tests were performed by applying both the indentation depth-time (*h*-*t*) relationship at the holding stage and the hardness, *H*, at various loading rates in order to explore the evolution of the strain rate sensitivity (SRS), *m*. The results obtained by tensile testing and nanoindentation are consistent despite the large difference in the volumes of the examined regions, thereby confirming the validity of using nanoindentation to measure the strain rate sensitivity.

Keywords: High-pressure torsion; Indentation creep; Nanoindentation; Pb-Sn alloy; Strain rate sensitivity

1. Introduction

Significant interest has developed over the last two decades in the processing of metals though the application of severe plastic deformation (SPD) where this leads to exceptional grain refinement to the submicrometer or even the nanometer range [1]. The two most attractive methods of SPD processing are equal-channel angular pressing (ECAP) [2] where a rod or bar is pressed through a die constrained within a channel bent through a sharp angle or high-pressure torsion (HPT) [3] where a disc is held between two massive anvils and subjected to a compressive load and concurrent torsional straining. Generally, HPT processing is the optimum procedure because experiments show that it produces ultrafine grains (UFG) that are smaller than in ECAP [4,5] and also it leads to a higher fraction of grain boundaries having high angles of misorientation [6].

The Pb-62% Sn eutectic alloy has a low absolute melting temperature, T_m, of about 456 K and often exhibits excellent superplastic properties due to the dual phase structure which inhibits grain growth at optimal superplastic temperatures above ~$0.5T_m$ [7,8]. Furthermore, this alloy is capable of exhibiting exceptional superplastic elongations of >7000% [9]. For this reason, the alloy is often used as a model material to investigate the characteristics of superplastic deformation under various experimental conditions. Recently, attention has been drawn to the issue of thermal stability of alloys processed by SPD and this becomes important when attempting to achieve superplastic elongations. For example, metals with relatively low stacking fault energies (SFE), such as Ag [10-12] and Cu [13-16], have attracted attention for investigations of the significance of self-annealing at room temperature (RT) after processing by ECAP or HPT. It is also reasonable to anticipate that alloys with low melting points such as Sn-based and Zn-based alloys will also exhibit self-annealing behaviour after SPD processing [17]. Accordingly, the primary objective of this

research was to investigate the evolution of both microstructure and flow behaviour in the Pb-Sn alloy during self-annealing following processing by HPT.

The strain rate sensitivity (SRS), *m*, is an important quantitative factor which holds the key to understanding the predominant mechanism in a stress-assisted, thermally-activated flow process [18-20]. For example, it is generally recognized that a high value of $m \approx 0.5$ together with tensile elongations of more than 400% are consistent with the occurrence of superplastic flow [21]. There are also numerous reports showing that ultrafine-grained bulk materials often exhibit exceptionally high strength at relatively low temperatures but with a significant decrease in their overall ductility [22,23]. However, by controlling the SRS it may be possible to delay the onset of localized deformation under tensile stresses resulting in improved ductilities [24,25].

Traditionally, the value of *m* is generally measured by recording the steady-state strain rate as a function of the applied stress but this approach requires conducting a large number of tensile tests with different strain rates or stresses and thus it entails the use of a relatively large volume of material. Recently, depth-sensing indentation (DSI) has become widely accepted as an alternative approach for mechanically characterizing bulk solids due to the associated simple sample preparation and the need for only a very small volume of testing material [26]. The use of DSI provides an opportunity for measuring the SRS using nanoindentation testing and recently there are reports describing the measuring of SRS from nanoindentation of various UFG metals including Al [27,28], Cu [28,29], Mg alloys [30,31], Ni [28], Sn-Ag-Cu [32], Zn-Al [28,33] a CoCrFeNiMn high-entropy alloy [34, 35] and an Al-Mg nanocomposite [36]. However, an evaluation shows that relatively little information is available comparing the values of the SRS measured for the same material using conventional tensile testing and nanoindentation and it is reasonable to anticipate that these two different straining conditions may affect the measurements of SRS. A second objective

of the present research was therefore to investigate the values recorded for the SRS in the Pb-Sn alloy processed by HPT using both tensile testing and nanoindentation testing and specifically to evaluate the significance of any evolution in the SRS during the self-annealing process.

2. Experimental material and procedures

The experiments were performed using a Pb-62% Sn eutectic alloy supplied as a cast billet and containing a binary microstructure with Pb-rich and Sn-rich phases. The alloy was machined into rods of 10 mm diameter and then cut into discs having thicknesses of ~1.2-1.5 mm. Each side of each disc was carefully polished to give a series of HPT disc samples having thicknesses of ~0.80 mm. Further information on the initial Pb-Sn alloy was given in an earlier report [37]. All discs were processed by HPT under quasi-constrained conditions in which there is a small outflow of material around the periphery of the disc during the processing operation [38]. The discs were processed for a total number, *N*, of 1 turn under a compressive pressure of 3.0 GPa using a rotation rate of 1 rpm. After HPT processing, the discs were stored at RT for different periods of time in order to examine the characteristics of self-annealing.

The HPT-processed discs were subsequently ground and polished with abrasive papers and diamond paste and, in order to reveal the grain boundaries, each polished disc was etched for 30-40 s in a solution of 25 ml H_2O, 5 ml HCl with a concentration of 37% and 5 g of NH_4HO_3. The nature of the various microstructures was systematically investigated during the course of storage using a scanning electron microscope (SEM) equipped with a high-brightness field emission gun (JEOL JSM-6500F). The average grain sizes were determined from the SEM images using separate measurements of at least ~300 individual grains. Prior to processing by HPT, the average grain sizes were measured as ~2.5 μm for both the Sn and Pb phases.

The conventional Vickers microhardness, *Hv*, at the edge of each disc was carefully monitored using a FM-300 microhardness tester with a maximum load of 10 gf and a dwell time of 15 s. The hardness values were recorded for up to 20 days after HPT processing until the hardness saturated at a reasonably stable value. These values were then converted to a recalculated Vickers microhardness, *Hrv*, in order to provide a meaningful comparison with the hardness values, *H*, obtained directly from the nanoindentation measurements. This conversion is necessary because in practice the conventional Vickers hardness value of *Hv* is defined as the maximum indentation load divided by the surface area of the indentation, A_S. Thus, this must be converted to *Hrv* which is defined as the peak load divided by the projected area of the indentation, A_P. It follows, therefore, that the conversion is given in the following simple form [39]:

$$Hrv = \frac{P_{\max}}{A_P} = \frac{2P_{\max}}{\mathrm{d_V}^2} = \frac{P_{\max}}{A_S \sin 68°} = \frac{Hv}{\sin 68°} \tag{1}$$

where P_{max} is the peak load, d_V is the diagonal of the Vickers indentation and the angle of 68° is based on a standard Vickers hardness indenter tip in a pyramidal shape with square base having an angle of 136° between the opposite faces. The SEM images of the indentation marks after Vickers microhardness measurements were also recorded using a dwell time of 5s in order to study the morphologies around the edges of the indents using samples both in the as-cast condition and after HPT processing.

Nanoindentation tests were undertaken at $r \approx 4.0$ mm where *r* is the distance from the centre in each disc at various time intervals during storage using an ultra-micro indentation system (UMIS) equipped with a three-sided pyramidal Berkovich indenter having a center-to-face angle of 65.3°. Both the loading stage and the holding (indentation creep) stage were used in this investigation to evaluate SRS by nanoindentation. For the indentation creep, the specimens were loaded to a fixed peak load of P_{max} = 5 mN at an indentation rate of 5×10^{-2}

mN s^{-1} and then a holding time of more than 2000 s was chosen to ensure that the creep was reasonably stable and steady-state flow was achieved. It is important to note that the selected indentation rate is not important when using this method because the SRS is measured by using depth-time (*h*-*t*) curves that start from the holding stage where the indentation rate is determined by factors such as the choice of material and the peak load.

For the first method of determining *m*, the creep behaviour which is reflected by the SRS at the holding stage in the nanoindentation test may be analyzed by the (*h*-*t*) relationship which is described by a power-law function of the form:

$$h = B(t - t_c)^{\frac{m}{2}} \tag{2}$$

where *B* and t_c are material-dependent constants: a detailed description of the origin of Eq. (2) was given in an earlier report [28]. In order to use this method, it is therefore necessary to fit Eq. (2) to the experimental *h*-*t* curves obtained for the holding stage in indentation creep and accordingly it is possible to determine the values of *B*, t_c and *m*/2. It should be noted that the power-law relationship in Eq. (2) is only valid if the *h*-*t* curves are obtained during the region of steady-state flow.

For the second method of determining *m* from the hardness values, *H*, obtained at different loading rates, the quantities of equivalent stress, σ_{eq}, and equivalent strain rate, $\dot{\varepsilon}_{eq}$, are used for a direct determination of SRS. Thus, the equivalent stress, σ_{eq}, is taken as one-third of the hardness value, *H*, and the equivalent strain rate, $\dot{\varepsilon}_{eq}$, at a given depth, *h*, for the indentation is then denoted by the relationship [40]:

$$\dot{\varepsilon}_{eq} = \frac{1}{h}\frac{dh}{dt}, \tag{3}$$

which is proportional to the loading rate. A range of equivalent strain rates from 1.1×10^{-4} to 4.3×10^{-3} s^{-1} was used in this analysis where the unloading stage occurred as soon as a maximum load of 50 mN was attained in order to record the hardness at the edge of the disc during self-annealing.

Finally, tensile tests were performed on HPT-processed samples for a direct and conventional evaluation of the SRS after storage at RT for periods of 1, 4 and 12 days. Electro-discharge machining was used to cut two tensile specimens from each disc with gauge lengths of 1.5 mm and cross-sectional areas of 1.0×0.6 mm^2. In order to avoid any microstructural inhomogeneities near the centres of the discs due to the HPT processing, these discs were cut from two symmetrical off-centre positions with the gauge lengths positioned so that their central points were 2.0 mm from the centre of each disc [41]. All tensile specimens were tested at RT using a Zwick machine operating at a constant rate of cross-head displacement with initial strain rates from 1.0×10^{-4} to 1.0×10^{-1} s^{-1}. These tests gave the flow stresses for different strain rates and thereby provided a direct measure of the SRS.

3. Experimental results

3.1 Evolution of microstructure and microhardness during self-annealing

Figure 1 shows SEM images of representative microstructures of the Pb-Sn alloy in (a) the as-cast condition and at the edge of a disc after processing by HPT for 1 turn and storing at RT for (b) 1 day, (c) 4 days and (d) 12 days: in these images, the dark grey phase represents Sn-rich and the light grey phase is Pb-rich. These four images use relatively low magnifications in order to include significant numbers of both the Sn-rich and Pb-rich phases, thereby providing overall representations of both the initial microstructure and the changes in microstructure occurring during storage. In Fig. 1(a) the initial as-cast microstructure consists of homogeneously distributed Sn-rich and Pb-rich phases and inspection shows there is no preferential alignment of either phase. However, processing by HPT introduces a banded structure in which agglomerates of both phases delineate the direction of torsional straining which is from the top to the bottom of the images in Figs 1(b), (c) and (d). Similar microstructural evolution was also reported in the Zn-22% Al eutectoid alloy after processing

by HPT [42,43]. It is evident from Fig. 1(b) that after a short storage time of 1 day the width of these banded phases is very small by comparison with the bands that are visible after storage times of 4 and 12 days in Figs 1(c) and (d), respectively.

Representative SEM images are shown in Fig. 2 at higher magnifications for the Pb-Sn alloy after HPT processing and storing for (a) 1 day and (b) 4 days. It is readily apparent from Fig. 2 that there is significant grain growth during storage. Specifically, the average grain size was ~1.5 μm after storage for 1 day of storage and ~1.9 μm after storage for 4 days. Moreover, significant agglomeration is visible with increasing storage time from 1 to 4 days in Fig. 2. Table 1 shows the measured average grain sizes during self-annealing up to 20 days where storage for 0 day denotes the grain size measured immediately after HPT processing. It should be noted that, for simplicity in measurements, these average grain sizes were determined from separate Sn grains but with the individual Pb-rich phases measured as a single grain even where there were indications from electron backscatter diffraction (EBSD) that the Pb-rich phase contained more than one grain within the Pb-Sn alloy [17]. This procedure is useful because it highlights the preferred interfaces for plastic deformation by grain boundary sliding (GBS) in the Pb-Sn alloy where most sliding occurs between Sn-Sn and Pb-Sn boundaries and there is little or no sliding at the Pb-Pb interfaces [44]. It is readily apparent from Table 1 that the grain size is immediately reduced from ~2.5 to ~1.3 μm by HPT processing through N = 1 turn but thereafter there is grain growth in RT storage and after 20 days the grain size is ~2.4 μm which is very close to the initial as-cast condition. Thus, these results of Figs 1 and 2 and Table 1 demonstrate that the grain size increases and the neighbouring phases agglomerate and form into larger phases with increasing self-annealing time.

Figure 3 shows the variations of the conventional Vickers microhardness values, *Hv*, (on the left axis) and the recalculated Vickers microhardness using Eq. (1) , *Hrv*, (on the right

axis), obtained at the edges of the discs after HPT processing through 1 turn and then storing at RT for up to 20 days. It should be noted that the values of *Hrv* obtained through Eq. (1) were multiplied by a factor of 9.807 to give units of MPa. The upper broken line at $Hv \approx 10$, which is equivalent to $Hrv \approx 107$ MPa, denotes the initial as-cast condition. Processing by HPT produces a significantly lower hardness of $Hrv \approx 17$ MPa and thereafter there is a rapid increase in hardness during the next 4 days to a value of ~56 MPa and then there is a slow increase in hardness to a maximum value of ~72 MPa after 20 days. Thus, all microhardness values recorded after HPT processing are significantly lower than in the as-cast condition. This decrease in hardness with HPT processing represents a weakening effect [45] and it is matched by results for some other materials such as the Zn-22% Al eutectoid alloy [37,42,43] and pure Pb, Sn and In [46].

The SEM images in Fig. 4 show the indentation marks taken after the Vickers microhardness measurements on the Pb-Sn alloy for (a) and (c) the as-cast condition and (b) and (d) at the edge of the disc after processing for 1 turn and storing for 12 days: the images in Figs 4(c) and (d) correspond to higher magnifications of the areas within the white boxes in Figs 4(a) and (b), respectively. Inspection shows that in the as-cast condition in Figs 4(a) and (c) the edges along the indent mark are very smooth and there is evidence for only a very limited amount or possibly no GBS. By contrast, the sample processed by HPT and stored for 12 days shows clear evidence for GBS with a pile-up of material along the edges of the indent in Figs 4(b) and (d). Pile-ups of material of this form are generally considered indicative of the occurrence of GBS as also recorded for other materials processed by ECAP [47-49]. Additionally, it is evident that most sliding appears to occur at the Sn-Sn and Pb-Sn interfaces which supports both earlier superplastic measurements [44] and the procedure adopted for measuring the grain sizes in Table 1. Thus, the microstructural observations suggest the occurrence of GBS in the HPT-processed samples at RT and therefore there is a

consequent loss of hardness due to GBS compared with the initial as-cast sample. A similar morphology of indent marks caused by GBS was reported recently in a Zn-22% Al eutectoid alloy processed by HPT through 4 turns and then subjected to nanoindentation testing [33].

3.2 SRS measured by nanoindentation at the holding stage

Representative load-displacement (*P*-*h*) curves from nanoindentation tests with a dwell time of 2000 s are shown in Fig. 5(a) where the curves are from tests performed on an as-cast sample and from the edge area of an HPT disc processed for one turn and stored at RT for 3, 10 and 12 days. The three stages of nanoindentation testing correspond to loading, creep at the holding condition and then unloading, where these stages are marked on the curve for the as-cast condition.

Two major trends are visible from these results. First, the displacements after unloading decrease significantly as the storage time increases in the HPT-processed samples. This is consistent with the hardness measurements in Fig. 3 where the hardness increases with increasing storage time. Second, there is a remarkably pronounced indentation creep during holding of the HPT-processed samples compared with the as-cast sample and the displacement during holding decreases as the storage time increases. In addition, noting the indentation depths of $h \approx 6.1$ μm after 3 days and ~5.1 μm after 12 days of storage in Fig. 5(a), it is easy to calculate that the diagonal lengths, *a*, of the indents for the HPT-processed sample decrease from ~46 μm after HPT and RT storage for 3 days to ~38 μm after processing and RT storage for 12 days where the lengths are given by $a = 2\sqrt{3}h\tan 65.3°$. Thus, combining this information with the microstructures in Fig. 1, it follows that the indent area should cover a sufficient number of grains so that the nanoindentation testing provides an average property of an area containing many grains rather than a single grain or phase. This conclusion is also consistent with the SEM images of the indents shown in Fig. 4.

Although the peak load was fixed at P_{max} = 5 mN, the equivalent strain rate, $\dot{\varepsilon}_{eq}$, during the holding stage should be different for each sample with different annealing conditions because of variations in the strength during storage. Therefore, it is necessary to examine these different strain rates if a method involving the holding stage is used to calculate the SRS. The equivalent strain rates calculated by Eq. (3) are plotted against the holding time in Fig. 5(b) for the samples already depicted in Fig. 5(a) where the insert shows a magnified view at a holding time of 700-1750 s. It is readily apparent from Fig. 5(b) that all tests enter essentially a steady-state flow after a holding time of ~700 s from the start of each test. It can be seen from the insert in Fig. 5(b) that the as-cast strain rate gradually decreases from ~5.0 × 10^{-5} to ~2.0 × 10^{-4} s^{-1} after reaching steady-state flow whereas the HPT-processed samples have higher strain rates from ~1.5 × 10^{-4} to ~4.0 × 10^{-4} s^{-1} but they are very close to each other.

Examples of fitted curves obtained using Eq. (2) are shown in Fig. 6 together with the experimental curves from the nanoindentation tests on the as-cast sample in Fig. 6(a) and a disc processed through 1 turn and stored at RT for 3, 10 and 12 days in Figs. 6(b), (c) and (d), respectively. The values and standard deviations of the fitting parameters B, t_c and n, which relate to m/2 as shown in Eq. (2), are also given in the lower right corners of each plot. Thus, all of the fitted curves start from 700 s of holding time to ensure that steady-state flow is achieved. Two conclusions are reached from close inspection of these various curves. First, all of the predicted curves from Eq. (2) fit exceptionally well with the experimental curves. Second, the SRS increases after HPT processing and as the storage time increases and this is independent of the decreases in the indentation depths in the HPT-processed samples.

3.3 SRS measured by nanoindentation at the loading stage

Examples of the load-displacement (P-h) curves are given in Fig. 7(a) with a maximum load of 50 mN for the samples after HPT for 1 turn, storing for 11 and 21 days and

testing by nanoindentation at different strain rates. The curves shown by the solid lines are for an HPT-processed disc stored for 11 days whereas the curves shown by the dashed lines are for an HPT-processed disc stored for 21 days. Three equivalent strain rates are shown corresponding to $\dot{\varepsilon}_{eq}$ of 1.9×10^{-3}, 4.0×10^{-4} and 2.3×10^{-4} s^{-1}. Two important trends are visible from these measurements. First, at any indentation strain rate the displacement at peak load is smaller for the sample stored for 21 days compared with the sample stored for 11 days. Second, there is a significant rate dependency of the peak-load displacement. Based on the *P*-*h* curves, the nanoindentation hardness, *H*, may be determined using the conventional procedure [50]. In Fig. 7(b), the variation of hardness with storage time is shown for different strain rates. It is generally evident that all curves have the same tendency at any given strain rate such that *H* increases with increasing storage time which is in agreement with Fig. 3. Furthermore, a faster strain rate leads to a higher hardness for all self-anneal conditions and thus a larger total of recovered hardness when compared to the hardness before HPT processing in the as-cast condition. It is important to note from Fig. 7(b) that all measurements for *H* are slightly lower at most given storage times than the recalculated hardness values, *Hrv*, obtained from the Vickers microhardness measurements shown in Fig. 3. Although there is an indentation size effect [51,52], the present difference arises primarily because the Vickers microhardness tests are conducted at a strain rate which is faster than any of the strain rates used in the nanoindentation tests and this higher load leads to higher values for the measured hardness.

The value of *m* may be determined from the slope of a straight line fit to the $\log \sigma_{eq} - \log \dot{\varepsilon}_{eq}$ data as shown in Fig. 8 for the HPT-processed samples with storage times of 2, 11 and 21 days. There is an evident tendency in Fig. 8 for the SRS to increase in 2 days after HPT with $m \approx 0.38$ compared with $m \approx 0.19$ in the as-cast condition shown in Fig. 6(a) and to further increase slightly to $m \approx 0.45$ with increasing storage time up to 21 days. This

result is directly consistent with the SRS measured in Fig. 6 at the holding stage. It is noted also from Fig. 8 that the slopes of the lines for 11 and 21 days start to decrease at strain rates above ~5.0×10^{-3} s^{-1}.

4. Discussion

4.1 The significance of self-annealing in the Pb-62% Sn alloy after processing by HPT

Processing by HPT generally produces a significant increase in hardness but in some limited numbers of materials, primarily those having low melting temperatures, the processing by HPT may produce a weakening effect so that the measured hardness is lower than in the initial condition [45]. The Pb-62% Sn eutectic alloy is an example of this weakening where the hardness is reduced substantially, by almost an order of magnitude, even after processing through only one HPT turn. Nevertheless, the present results demonstrate the occurrence of very significant self-annealing after storage at RT with a rapid increase in hardness over the first 4 days as shown in Fig. 3 and then a gradual increase in hardness during further storage.

When recording values of the Vickers microhardness on the surfaces of the Pb-Sn samples, the measuring procedure produces well-defined indentation marks that provide additional evidence regarding the nature of the flow process. Close inspection of these indents suggests the occurrence of grain boundary sliding in this alloy at RT, as shown by the presence of material pile-ups around the indent in Fig. 4(d). This conclusion is reasonable because, due to the very low melting temperature of the Pb-Sn alloy (456 K), room temperature corresponds to an homologous temperature of ~$0.65T_m$ and, consistent with this high temperature, earlier experimental results demonstrated the occurrence of excellent superplastic properties in this alloy when testing in tension at low strain rates with tensile elongations at RT up to and exceeding 2000% [53,54].

4.2 A comparison of the different procedures used to measure the SRS

The values of the SRS measured by tensile testing at RT over the strain rate range from 1.0×10^{-4} to 1.0×10^{-1} s^{-1} are summarized in Table 2 using incremental values of strain rate of one order of magnitude. These results are for the as-cast condition and after HPT and storage at RT for totals of 1, 4 and 12 days. It is readily apparent from this tabulation that, for the HPT-processed samples, the peak SRS shifts towards lower strain rates as the storage time increases. Thus, the peak *m* of ~0.45 shifts from $1.0 \times 10^{-3} – 1.0 \times 10^{-2}$ s^{-1} after 1 day of storage to $1.0 \times 10^{-4} – 1.0 \times 10^{-3}$ s^{-1} after 12 days of storage.

This shift is better delineated when the *m* values are plotted against the maximum strain rate of the strain rate range in which the SRS was measured, as shown by the open points for the tensile tests in Fig. 9. Using these data, and combining with the grain size measurements recorded in Table 1, it is evident that the peak in the SRS shifts from a strain rate of 1.0×10^{-2} s^{-1} to 1.0×10^{-3} s^{-1} as the grain size increases during storage from ~1.5 to ~2.3 μm during self-annealing from 1 to 12 days.

In addition to the measured SRS from tensile tests as shown by the open points in Fig. 9, data are included also for nanoindentation at both holding and loading as denoted by the semi-solid and the solid symbols, respectively: for ease of comparison, datum points measured at reasonably similar storage times have symbols with the same shape so that the datum point measured at holding after 12 days and the datum point measured at loading after 11 days are both denoted by a square. The datum points measured at loading are placed in Fig. 9 in the strain rate region from $1.0 \times 10^{-4} – 1.0 \times 10^{-3}$ s^{-1} because it is evident from Fig. 8 that the SRS drops at faster strain rates. For the datum points measured at holding, the strain rate range covered less than an order of magnitude and this is limited by the method of testing since the strain rate is not a controllable factor. However, it is reasonable to place these points in Fig. 9 at the starting strain rates for steady-state flow which are also the maximum strain rates where the SRS was measured.

Combining these various procedures in the presentation in Fig. 9, it is apparent that there is a very good match between the SRS measured by tensile tests and by the nanoindentation tests for both holding and loading. Thus, the datum points measured at loading after 2 and 11 days are very close to the tensile measurements and the datum points measured at holding show excellent agreement with the trends predicted by the tensile tests which in turn add more evidence to a shift in the SRS peak due to grain growth.

Finally, it should be noted that the nanoindentation results obtained from both the holding and the loading stages in Figs 6 and 8 suggest that *m* increases with increasing storage time and therefore with increasing grain size. Initially, this appears unreasonable but it is readily apparent from Fig. 9 that the increase of *m* with increasing grain size is due to the shift in the SRS peak during self-annealing so that, for fine-grained samples, the peak of SRS moves towards faster strain rates due to the grain refinement. These results show that, for alloys with very low melting points such as the Pb-Sn alloy, many properties at RT such as strength, microhardness and the values of the SRS should be compared at a specific strain rate because at this high homologous temperature the mechanical properties are critically affected by the testing strain rate.

5. Summary and conclusions

1. A Pb-62% Sn eutectic alloy was processed by HPT for one turn at RT. Hardness measurements showed there was a weakening after HPT processing but the hardness increased due to self-annealing during subsequent storage at RT. Grain growth also occurred during storage at RT.

2. A direct comparison of the SRS measured by tensile tests and nanoindentation tests, both at the holding and the loading stage, showed that all techniques give consistent values for *m*. There is also a peak in the SRS which shifts to slower strain rates with increasing

storage time leading to increasing grain size in both the tensile tests and the nanoindentation tests.

Acknowledgements

This work was supported in part by NRF Korea funded by MoE under Grant No. NRF-2014R1A1A2057697 (MK), in part by the Hungarian Scientific Research Fund (OTKA) under Grants K109570 and K109021 (NQC) and in part by the European Research Council under ERC Grant Agreement No. 267464-SPDMETALS (NXZ, YH, TGL).

References

[1] T.G. Langdon, Twenty-five years of ultrafine-grained materials: achieving exceptional properties through grain refinement, Acta Mater. 61 (2013) 7035–7059.

[2] R.Z. Valiev, T.G. Langdon, Principles of equal-channel angular pressing as a processing tool for grain refinement, Prog. Mater. Sci. 51 (2006) 881–981.

[3] A.P. Zhilyaev, T.G. Langdon, Using high-pressure torsion for metal processing: Fundamentals and applications, Prog. Mater. Sci. 53 (2008) 893–979.

[4] A.P. Zhilyaev, B.K. Kim, G.V. Nurislamova, M.D. Baró, J.A. Szpunar, T.G. Langdon, Orientation imaging microscopy of ultrafine-grained nickel, Scr. Mater. 46 (2002) 575–580.

[5] A.P. Zhilyaev, G.V. Nurislamova, B.K. Kim, M.D. Baró, J.A. Szpunar, T.G. Langdon, Experimental parameters influencing grain refinement and microstructural evolution during high-pressure torsion, Acta Mater. 51 (2003) 753–765.

[6] J. Wongsa-Ngam, M. Kawasaki, T.G. Langdon, A comparison of microstructures and mechanical properties in a Cu-Zr alloy processed using different SPD techniques, J. Mater. Sci. 48 (2013) 4653–4660.

[7] F.A. Mohamed, T.G. Langdon, Creep behaviour in the superplastic Pb-62% Sn eutectic, Phil. Mag. 32 (1975) 697-709.

[8] M.M.I. Ahmed, T.G. Langdon, Exceptional ductility in the Pb-62 pct Sn eutectic, Metall. Trans. A 8A (1977) 1832-1833.

[9] Y. Ma, T.G. Langdon, Factors influencing the exceptional ductility of a Pb-62 pct Sn alloy, Metall. Mater. Trans. A 25A (1994) 2309-2311.

[10] J. Gubicza, N. Q. Chinh, J. L. Lábár, Z. Hegedűs, T.G. Langdon, Principles of self-annealing in silver processed by equal-channel angular pressing: The significance of a very low stacking fault energy, Mater. Sci. Eng. A527 (2010) 752-760.

[11] Z. Hegedüs, J. Gubicza, M. Kawasaki, N.Q. Chinh, J.L. Lábár, T.G. Langdon, Stability of the ultrafine-grained microstructure in silver processed by ECAP and HPT, J. Mater. Sci. 48 (2013) 4637-4645.

[12] Z. Hegedűs, J. Gubicza, P. Szommer, N. Q. Chinh, Y. Huang, T.G. Langdon, Inhomogeneous softening during annealing of ultrafine-grained silver processed by HPT, J. Mater. Sci. 48 (2013) 7384-7391.

[13] O. V. Mishin, A. Godfrey, Microstructure of ECAE-processed copper after long-term room-temperature storage, Metall. Mater. Trans. A 39A (2008) 2923-2930.

[14] A.I. Almazrouee, K.J. Al-Fadhalah, S.N. Alhajeri, T.G. Langdon, Microstructure and microhardness of OFHC copper processed by high-pressure torsion, Mater. Sci. Eng. A641 (2015) 21–28.

[15] J. Xu, J. Li, C.T. Wang, D. Shan, B. Guo, T.G. Langdon, Evidence for an early softening behaviour in pure copper processed by high-pressure torsion, J. Mater. Sci. 51 (2016) 1923–1930.

[16] Y. Huang, S. Sabbaghianrad, A.I. Almazrouee, K.J. Al-Fadhalah, S.N. Alhajeri, T.G. Langdon, The significance of self-annealing at room temperature in high purity copper processed by high-pressure torsion, Mater. Sci. Eng. A656 (2016) 55-66.

[17] N.X. Zhang, M. Kawasaki, Y. Huang, T.G. Langdon, The significance of self-annealing in two-phase alloys processed by high-pressure torsion, IOP Conf. Ser.: Mater. Sci. Eng. 63 (2014) 012126 (1-9).

[18] L. Lu, R. Schwaiger, Z.W. Shan, M. Dao, K. Lu, S. Suresh, Nano-sized twins induce high rate sensitivity of flow stress in pure copper, Acta Mater. 53 (2005) 2169-2179.

[19] R.J. Asaro, S. Suresh, Mechanistic models for the activation volume and rate sensitivity in metals with nanocrystalline grains and nano-scale twins, Acta Mater. 53 (2005) 3369-3382.

[20] Y.M. Wang, A. V. Hamza, E. Ma, Temperature-dependent strain rate sensitivity and activation volume of nanocrystalline Ni, Acta Mater. 54 (2006) 2715-2726.
[21] T.G. Langdon, Seventy-five years of superplasticity: historic developments and new opportunities, J. Mater. Sci. 44 (2009) 5998-6010.
[22] R.Z. Valiev, I.V. Alexandrov, Y.T. Zhu, T.C. Lowe, Paradox of strength and ductility in metals processed by severe plastic deformation, J. Mater. Res. 17 (2002) 5–8.
[23] P. Kumar, M. Kawasaki, T.G. Langdon, Review: Overcoming the paradox of strength and ductility in ultrafine-grained materials at low temperatures, J. Mater. Sci. 51 (2016) 7-18.
[24] Y.T. Zhu, X. Liao, Nanostructured metals - Retaining ductility, Nat. Mater. 3 (2004) 351-352.
[25] T. Mungole, P. Kumar, M. Kawasaki, T.G. Langdon, A critical examination of the paradox of strength and ductility in ultrafine-grained metals, J. Mater. Res. 29 (2014) 2534–2546.
[26] L.H. He, M.V. Swain, Nanoindentation creep behavior of human enamel, J. Biomed, Mater. Res. 91A (2009) 352-359.
[27] N.Q. Chinh, T. Csanádi, T. Győri, R.Z. Valiev, B.B. Straumal, M. Kawasaki, T.G. Langdon, Strain rate sensitivity studies in an ultrafine-grained Al-30 wt.% Zn alloy using micro-and nanoindentation, Mater. Sci. Eng. A543 (2012) 117-120.
[28] N.Q. Chinh, P. Szommer, Mathematical description of indentation creep and its application for the determination of strain rate sensitivity, Mater. Sci. Eng. A611 (2014) 333-336.
[29] I.C. Choi, Y.J. Kim, Y.M. Wang. U. Ramamurty, J.I. Jang, Nanoindentation behavior of nanotwinned Cu: Influence of indenter angle on hardness, strain rate sensitivity and activation volume, Acta Mater. 61 (2013) 7313-7323.
[30] H. Somekawa, C.A. Schuh, Effect of solid solution elements on nanoindentation hardness, rate dependence, and incipient plasticity in fine grained magnesium alloys, Acta Mater. 59 (2011) 7554-7563.
[31] I.C. Choi, D.H. Lee, B. Ahn, K. Durst, M. Kawasaki, T.G. Langdon, J.I. Jang, Enhancement of strain-rate sensitivity and shear yield strength of a magnesium alloy processed by high-pressure torsion, Scr. Mater. 94 (2015) 44-47.
[32] G. Xiao, G. Yuan, C. Jia, X. Yang, Z. Li, X. Shu, Strain rate sensitivity of Sn–3.0Ag–0.5Cu solder investigated by nanoindentation, Mater. Sci. Eng. A613 (2014) 336-339.
[33] I.C. Choi, Y.J. Kim, B. Ahn, M. Kawasaki, T.G. Langdon, J.I. Jang, Evolution of plasticity, strain-rate sensitivity and the underlying deformation mechanism in Zn-22% Al during high-pressure torsion, Scr. Mater. 75 (2014) 102-105.
[34] D.H. Lee, I.C. Choi, M.Y. Seok, J. He, Z. Lu, J.Y. Suh, M. Kawasaki, T.G. Langdon, J.I. Jang, Nanomechanical behavior and structural stability of a nanocrystalline CoCrFeNiMn high-entropy alloy processed by high-pressure torsion, J. Mater. Res. 30 (2015) 2804-2815.
[35] D.H. Lee, M.Y. Seok, Y. Zhao, I.C. Choi, J. He, Z. Lu, J.Y. Suh, U. Ramamurty, M. Kawasaki, T.G. Langdon, J.I. Jang, Spherical nanoindentation creep behavior of nanocrystalline and coarse-grained CoCrFeMnNi high-entropy alloy, Acta Mater. 109 (2016) 314-322.
[36] B. Ahn, H.-J. Lee, I.C. Choi, M. Kawasaki, J.I. Jang, T.G. Langdon, Micro-mechanical behavior of an exceptionally strong metal matrix nanocomposite processed by high-pressure torsion, Adv. Eng, Mater. (in press) DOI: 10.1002/adem.201500520
[37] N.X. Zhang, M. Kawasaki, Y. Huang, T.G. Langdon, Microstructural evolution in two-phase alloys processed by high-pressure torsion, J. Mater. Sci. 48 (2013) 4582-4591.
[38] R.B. Figueiredo, P.H.R. Pereira, M.T.P. Aguilar, P.R. Cetlin, T.G. Langdon, Using

finite element modelling to examine the temperature distribution in quasi- constrained high-pressure torsion, Acta Mater. 60 (2012) 3190–3198.
[39] J.-I. Jang, S. Shim, S.-I. Komazaki, T. Honda, A nanoindentation study on grain-boundary contributions to strengthening and aging degradation mechanisms in advanced 12 Cr ferritic steel, J. Mater. Res. 22 (2007) 175-185.
[40] C. Fisher-Cripps, *Nanoindentation*, 2nd ed., (Springer-Verlag, NewYork, 2004), p. 146.
[41] A. Loucif, R.B. Figueiredo, M. Kawasaki, T. Baudin, F. Brisset, R. Chemam, T.G. Langdon, Effect of aging on microstructural development in an Al-Mg-Si alloy processed by high-pressure torsion, J. Mater. Sci. 47 (2012) 7815-7820.
[42] M. Kawasaki, B. Ahn, T. G. Langdon, Microstructural evolution in a two-phase alloy processed by high-pressure torsion, Acta Mater 58 (2010) 919-930.
[43] M. Kawasaki, B. Ahn, T.G. Langdon, Significance of strain reversals in a two-phase alloy processed by high-pressure torsion, Mater. Sci. Eng. A527 (2010) 7008-7016.
[44] R.B. Vastava, T.G. Langdon, An investigation of intercrystalline and interphase boundary sliding in the superplastic Pb-62% Sn eutectic, Acta Metall. 27 (1979) 251-257.
[45] M. Kawasaki, Different models of hardness evolution in ultrafine-grained materials processed by high-pressure torsion, J. Mater. Sci. 49 (2014) 18-34.
[46] K. Edalati, Z. Horita, Significance of homologous temperature in softening behavior and grain size of pure metals processed by high-pressure torsion, Mater. Sci. Eng. A528 (2011) 7514-7523.
[47] N.Q. Chinh, P. Szommer, Z. Horita, T.G. Langdon, Experimental evidence for grain-boundary sliding in ultrafine-grained aluminium processed by severe plastic deformation, Adv. Mater. 18 (2006) 34-39.
[48] V. Maier, B. Merle, M. Göken, K. Durst, An improved long-term nanoindentation creep testing approach for studying the local deformation processes in nanocrystalline metals at room and elevated temperatures, J. Mater. Res. 28 (2013) 1177-1188.
[49] J.M. Wheeler, V. Maier, K. Durst, M. Göken, J. Michler, Activation parameters for deformation of ultrafine-grained aluminium as determined by indentation strain rate jumps at elevated temperature, Mater. Sci. Eng. A585 (2013) 108-113.
[50] W.C. Oliver, G.M. Pharr, An improved technique for determining hardness and elastic modulus using load and displacement sensing indentation experiments, J. Mater. Res. 7 (1992) 1564-1583.
[51] W.D. Nix, H. Gao, Indentation size effects in crystalline materials: A law for strain gradient plasticity, J. Mech. Phys. Solids 46 (1998) 411-425.
[52] G.M. Pharr, E.G. Herbert, Y. Gao, The indentation size effect: A critical examination of experimental observations and mechanistic interpretations, Ann. Rev. Mater. Res. 40 (2010) 271-292.
[53] M.M.I. Ahmed, T.G. Langdon, Ductility of the Pb-Sn eutectic at room temperature, J. Mater. Sci. Lett. 2 (1983) 59-62.
[54] M.M.I. Ahmed, T.G. Langdon, The effect of grain size on ductility in the superplastic Pb-Sn eutectic, J. Mater. Sci. Lett. 2 (1983) 337-340.

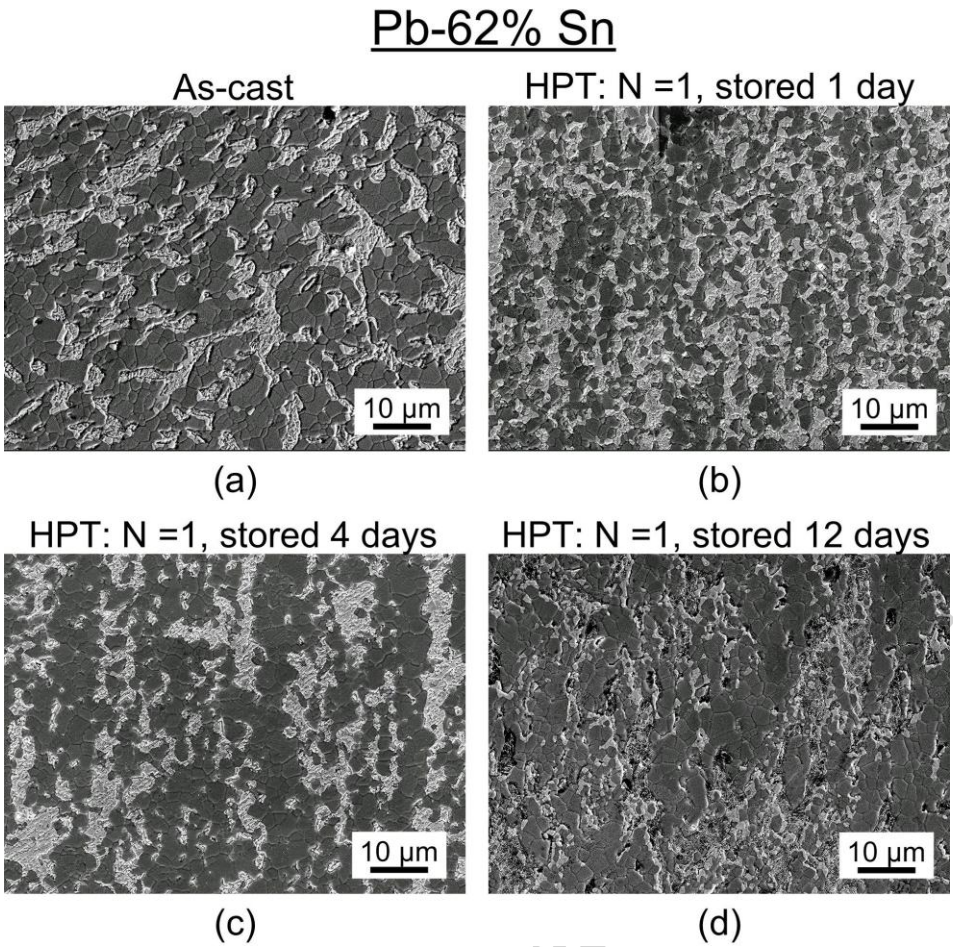

Fig. 1 Representative SEM images for (a) the as-cast condition and at the edges of the discs after HPT for 1 turn and storage for (b) 1 day, (c) 4 days and (d) 12 days.

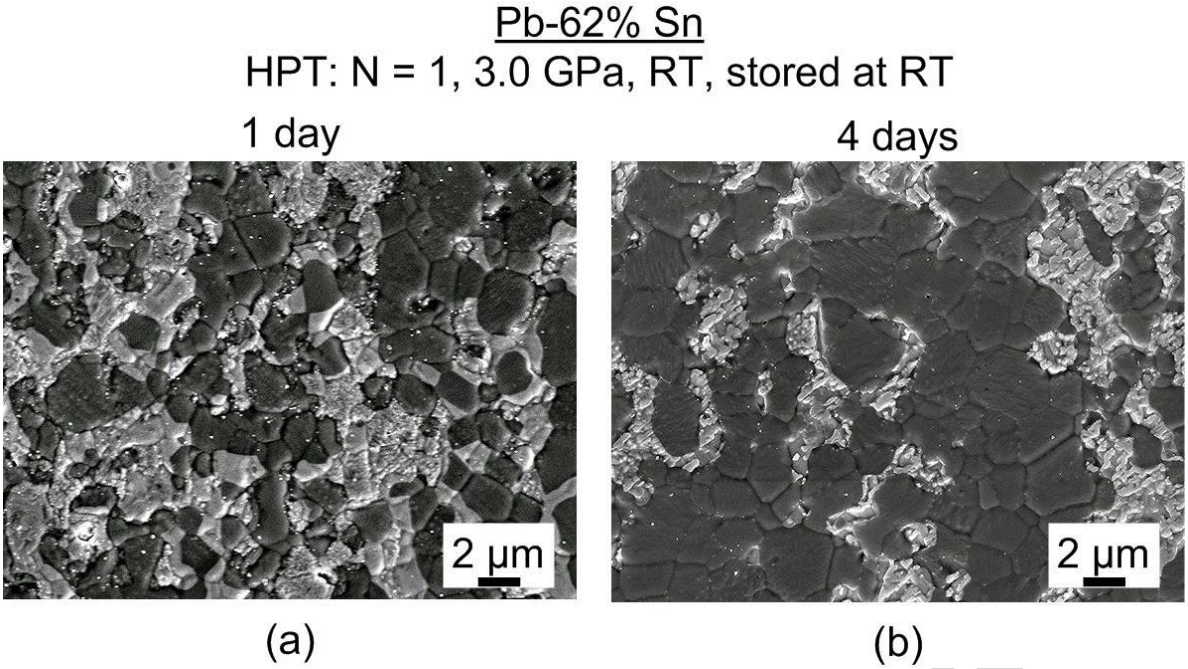

Fig. 2 Detailed SEM images taken at the edge of a disc after HPT for 1 turn and storage for (a) 1 day and (b) 4 days.

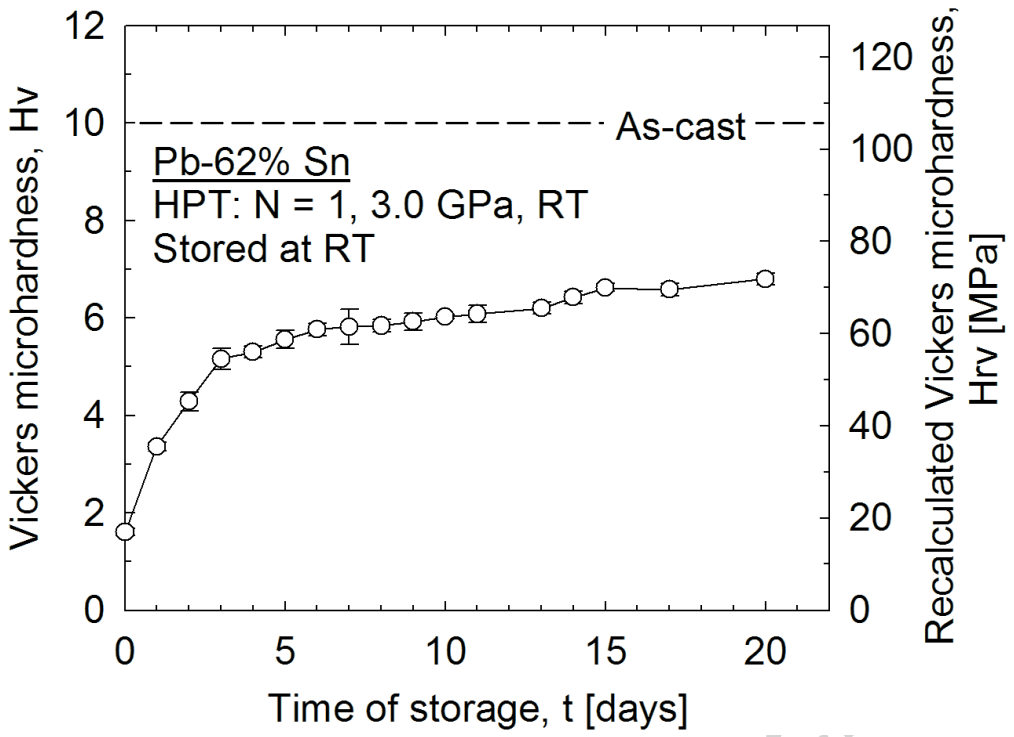

Fig. 3 Variation of the measured hardness values at the edge of a disc after HPT for 1 turn with time of storage up to 20 days: the recalculated Vickers microhardness (in MPa) is shown on the right.

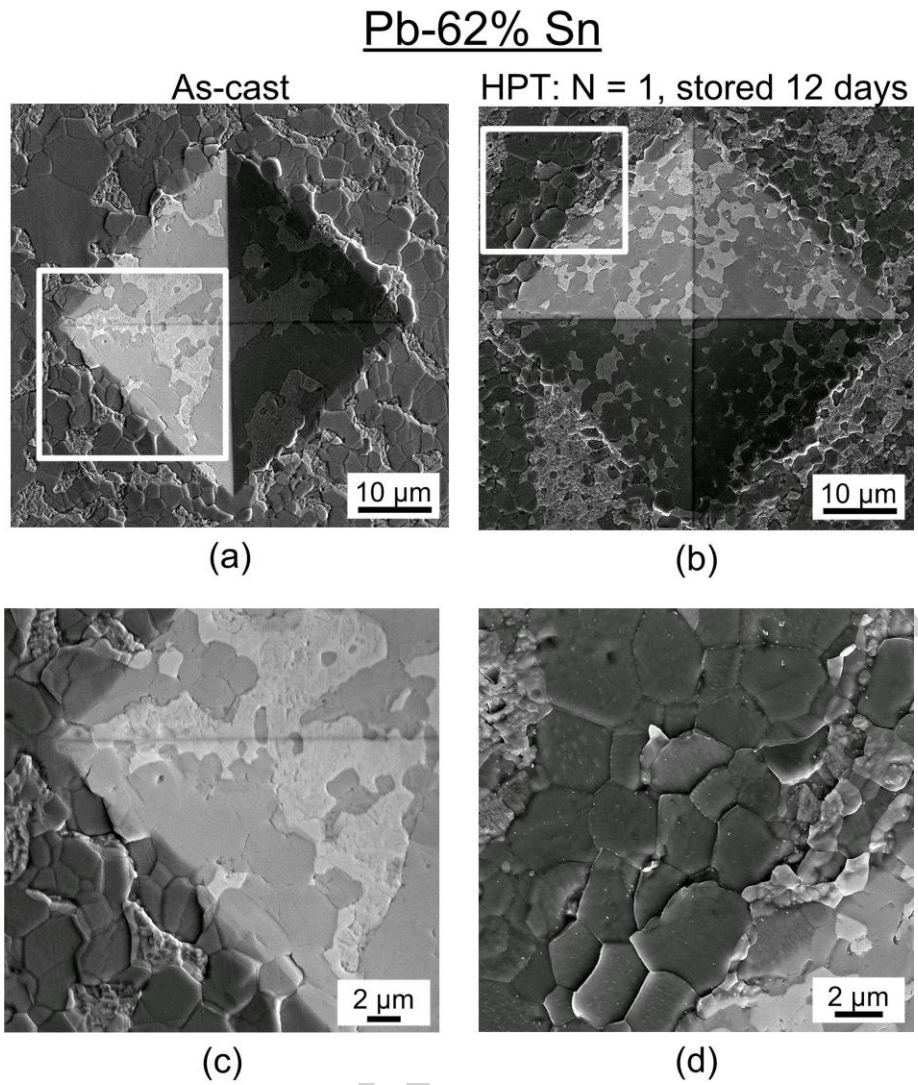

Fig. 4 SEM images showing the indent marks after Vickers microhardness measurements taken at the edges of the Pb-Sn discs (a) in the as-cast condition and (b) after processing by HPT for 1 turn and storing at RT for 12 days: (c) and (d) are higher magnification images showing the areas denoted by the white boxes in (a) and (b).

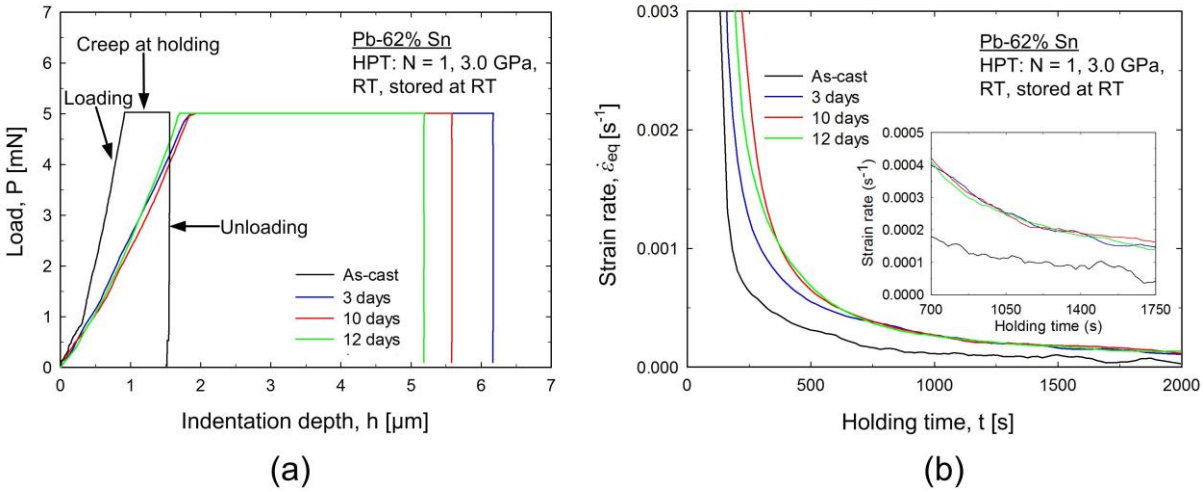

Fig. 5 (a) Typical *P-h* curves obtained after different storage times for a disc processed by HPT for 1 turn and (b) the calculated strain rates for different storage times.

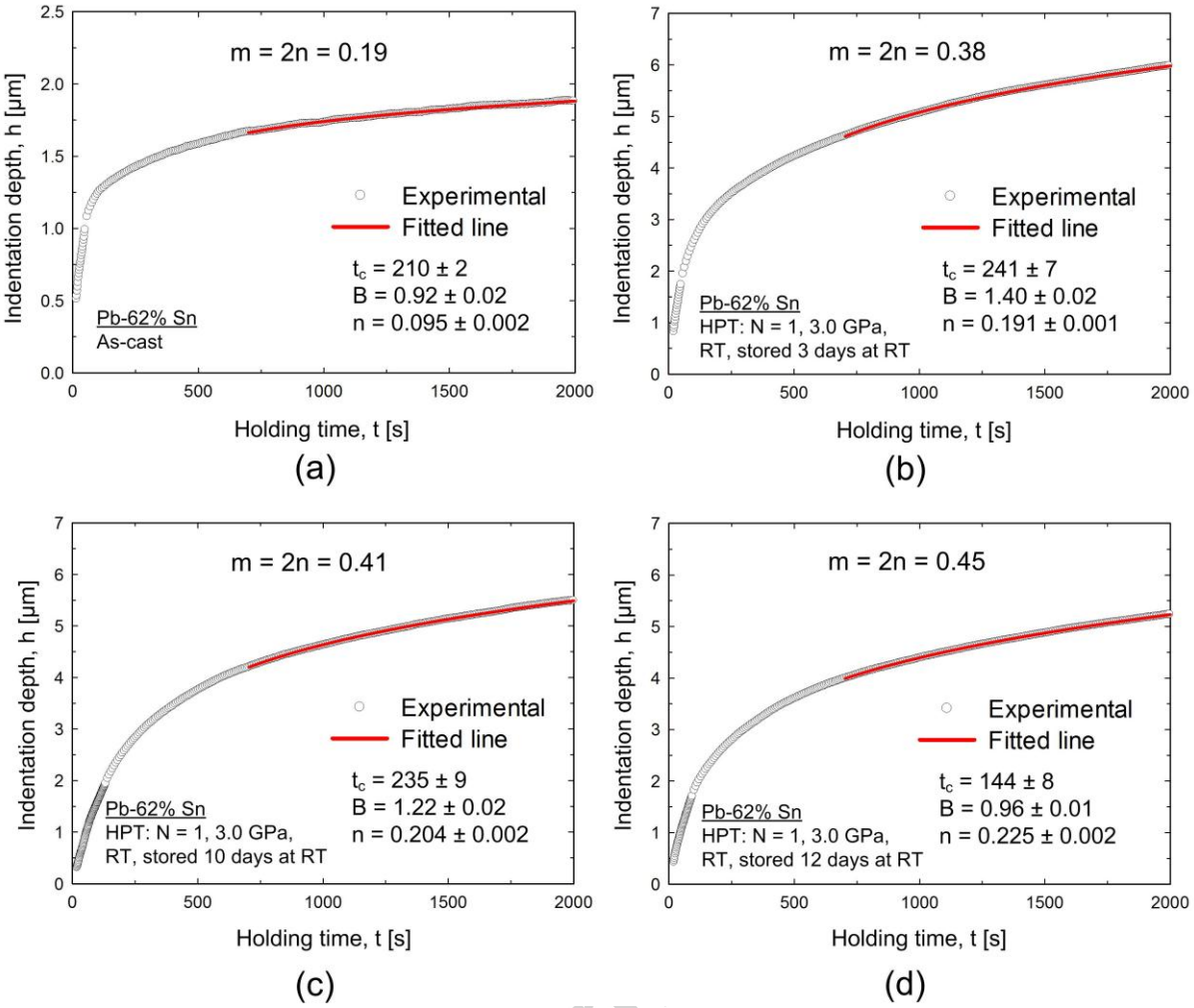

Fig. 6 Examples of using Eq. (2) to determine the values of *m* in (a) the as-cast condition and for a disc processed by HPT for 1 turn and stored at RT for (b) 3, (c) 10 and (d) 12 days.

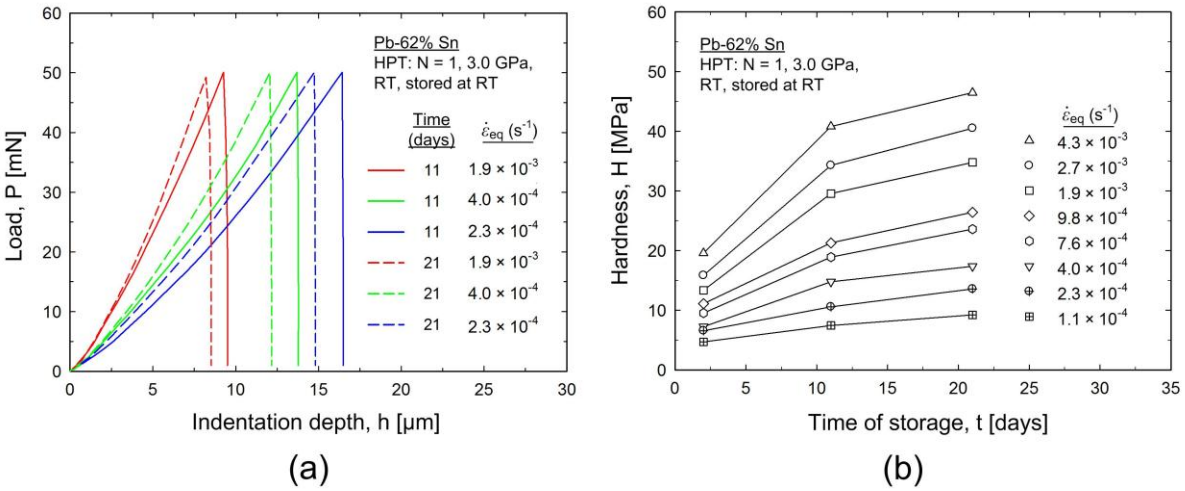

Fig. 7 (a) Typical *P-h* curves obtained from storage times of 11 and 21 days for a disc processed by HPT for 1 turn and (b) the hardness variation with increasing storage time.

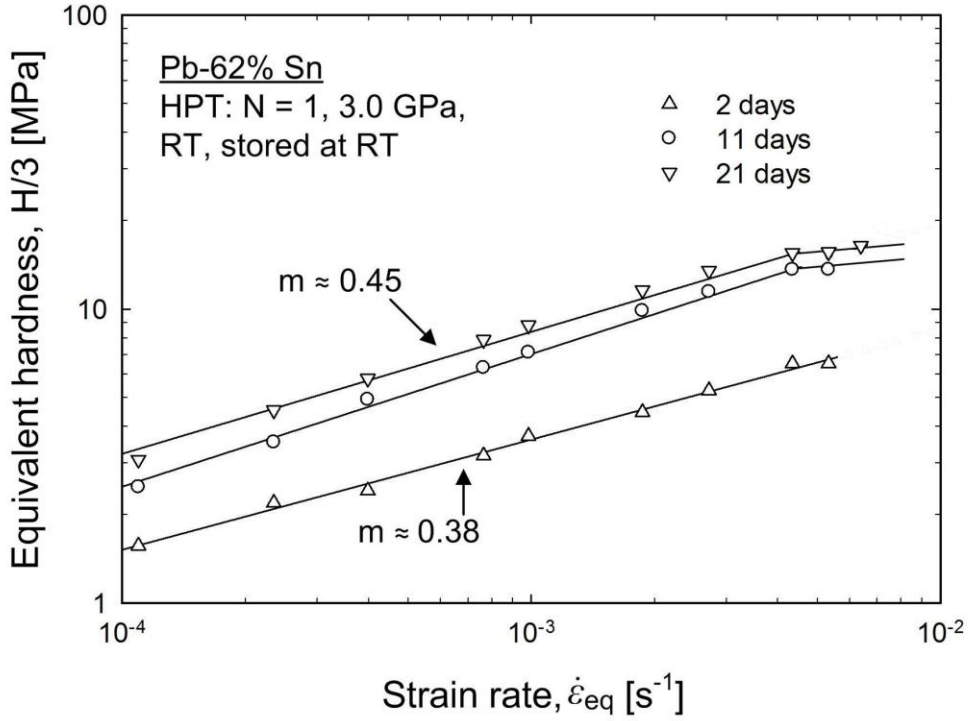

Fig. 8 An evaluation of SRS for a disc processed by HPT for 1 turn and stored at RT for 2, 11 and 21 days.

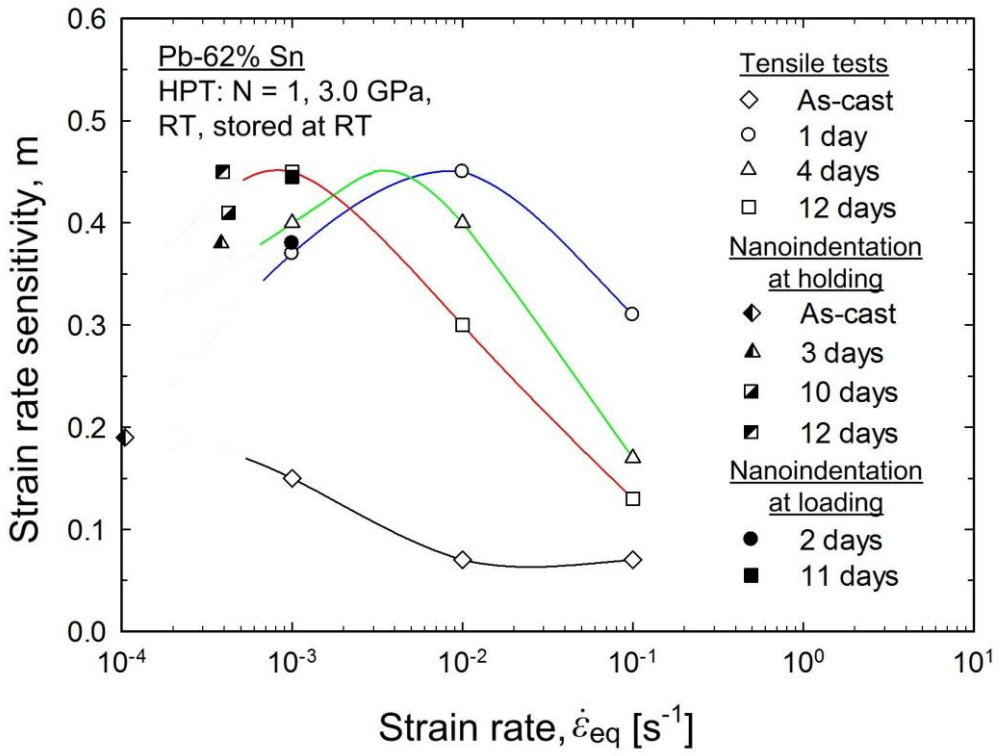

Fig. 9 SRS obtained from tensile tests and nanoindentation tests at both the holding and loading stage plotted against the maximum strain rate in the range where the SRS was measured: identical shapes of symbols are used for similar storage times.

Table 1 Average grain size after storage

Time (days)	0	1	2	4	6	11	12	20
d (μm)	~1.3	~1.5	~1.8	~1.9	~2.0	~2.2	~2.3	~2.4

Table 2 SRS measured by tensile testing at RT

Strain rate range (s^{-1})	As-cast	1 day	4 days	12 days
$1.0 \times 10^{-4} – 1.0 \times 10^{-3}$	0.15	0.37	0.40	0.45
$1.0 \times 10^{-3} – 1.0 \times 10^{-2}$	0.07	0.45	0.40	0.30
$1.0 \times 10^{-2} – 1.0 \times 10^{-1}$	0.07	0.31	0.17	0.13